J. Synchrotron Rad. (1999). **6**, 865–874

Bluetongue virus: the role of synchrotron radiation

Jonathan M. Diprose,[a]* Jonathan M. Grimes,[a] Patrice Gouet,[a]† Robyn Malby,[a]‡ J. Nicholas Burroughs,[b] Julien Lescar,[c] Bjarne Rassmussen,[d] Peter P. C. Mertens[b] and David I. Stuart[a,e]

[a]The Laboratory of Molecular Biophysics, Biochemistry Department, University of Oxford, Rex Richards Building, South Parks Road, Oxford OX1 3QU, UK, [b]The Institute for Animal Health, Pirbright Laboratory, Ash Road, Pirbright, GU24 0NF, UK, [c]ESRF, BP 220, 38043 Grenoble CEDEX 9, France, [d]EMBL Grenoble Outstation, c/o ILL, BP 156, 38042 Grenoble CEDEX 9, France, and [e]The Oxford Centre for Molecular Sciences, University of Oxford, New Chemistry Laboratory, South Parks Road, Oxford OX1 3QT, UK. E-mail: jonathand@biop.ox.ac.uk

(*Received 15 April 1999; accepted 12 May 1999*)

The determination of the structure of the transcriptionally active core particle of bluetongue virus is discussed. This particle is approximately 700 Å in diameter and reasonably well ordered, but fragile, crystals have been obtained from two different serotypes of the virus. Cryocrystallography proved difficult and a large number of crystals were analysed at room temperature to accumulate a reasonably complete data set. The effects of synchrotron optics, station design and detector on the signal-to-noise for these weak data are discussed, with particular reference to station ID2 at the European Synchrotron Radiation Facility. Once the data had been gathered, structure determination was straightforward, using a model derived from a combination of electron microscopy and protein crystallography to obtain initial phases. Despite apparent isomorphism, it is suspected that the crystal lattice 'ages', perhaps reflecting both the inevitable weakness of the forces holding crystals of such a large macromolecular complex together and flexibility in the particle.

Keywords: virus structure; macromolecular crystallography; large unit cells; third-generation sources; bluetongue virus.

1. Introduction

Bluetongue virus (BTV) possesses an icosahedral non-enveloped capsid roughly 800 Å in diameter. It has a segmented dsRNA genome and so, to protect itself from the cellular defence responses which are extremely intolerant of dsRNA, the virus genome is kept wrapped up safely even after entry into the cell, within the so-called core particle. This strategy is quite different to most other viruses, which simply unload their genomes within the appropriate cellular compartment as efficiently and quickly as possible. As a consequence of this lifestyle, the BTV core particle contains not only the segmented genome but all the enzymes needed for production of fully capped messenger RNA (mRNA), which are made within the particle and then secreted into the cytoplasm of the infected cell. The core particle has two protein layers, an outer shell made up of 780 copies of VP7(T13) (MW 38 kDa) (arranged as trimers on a $T = 13$ lattice) clothes an inner layer of 120 copies of VP3(T2) (MW 106 kDa). The inner layer has an arrangement apparently unique to dsRNA viruses (Grimes *et al.*, 1998). Within this layer are copies of a helicase, a dsRNA dependant ssRNA polymerase and methyl and guanylyl transferases (Ramadevi *et al.*, 1998; Stauber *et al.*, 1997; Urakawa *et al.*, 1989), which associate with each other to form transcription complexes, one of which is associated with each of the ten segements of the dsRNA genome. Some aspects of the life cycle are shown schematically in Fig. 1.

Here we present an overview of the structural analysis of BTV cores. Our primary focus is the analysis of BTV-1 SA, which crystallizes in space group $P2_12_12$, with approximate cell dimensions a = 796 Å, b = 822 Å, c = 753 Å and possesses one-half of a core in the crystallographic asymmetric unit (Burroughs *et al.*, 1995). Where appropriate, we will also mention the analysis of BTV-10 USA, whose crystals belong to space group $P4_12_12$ (cell dimensions a = 1115 Å, b = 1115 Å, c = 1584 Å) with a whole core in the crystallographic asymmetric unit (Gouet *et al.*, 1999).

2. Crystals

Bluetongue virus does not contain a lipid envelope. However, it can wrap itself in the cell's outer membrane and bud from the cell surface, forming membrane-envel-

† Present address: CNRS-IPBS, Group de Cristallographie Biologique, 205 Route de Narbonne, 31077 Toulouse, France.
‡ Present address: Biomolecular Research Institute, 343 Royal Parade, Parkville Victoria 3052, Australia.

oped virus particles (MEVP) (Martin *et al.*, 1998). Although MEVP are unstable and the envelope is rapidly lost, there remains a close association between the virion and cell debris/membranes, which initially prevented the development of effective purification methods for large quantities of virus particles. A specific range of detergents were identified that do not disrupt the virus and which, if used together with a reducing agent (such as DTT), or proteases (such as chymotrypsin or trypsin), efficiently solubilize infected cell debris (Burroughs *et al.*, 1994; Mertens *et al.*, 1987). Intact BTV particles, or protease-modified infectious subviral particles (ISVP), that are released by such treatment are then purified by centrifugation. The outer capsid of BTV and related viruses can be released by metal ions, for example by treatment with $MgCl_2$ or CsCl (Van Dijk & Huismans, 1980). Centrifugation of the released virus particles, or ISVP, on CsCl gradients, therefore removes components of the BTV outer capsid to release the virus cores, which then form a band of pure cores (Fig. 2). Development of these techniques allowed us to scale up production methods to generate sufficient BTV particles for crystallization trials and structural studies (Burroughs *et al.*, 1995). However, the purity of each core preparation remains a major factor in the size, number and quality of the BTV core crystals that can be generated, even under otherwise standard conditions. This underlines the importance in our structural studies of effective purification methods that generate a homogeneous product. It is possible to purify approximately 40 mg of virus particles, or 20 mg of BTV cores, from 40 roller bottles. A single-sitting drop may generate 1–5 large crystals (up to 0.5 mm in diameter); however, most drops generate useless aggregates or no crystals at all. Since each crystal usually only yields a single small oscillation range diffraction image, virus and core particle production represents a continuing effort that underlies the whole of our strategy for the structural analysis of the BTV.

Crystals take a number of months to grow and then appear to be stable for over a year. The crystallization process is relatively standard, although crystals are grown at a somewhat elevated temperature (Burroughs *et al.*, 1995), presumably due to the essential insolubility of the particles at 277 K. Crystals were pre-mounted in quartz capillaries prior to transport to the synchrotron to conform to the guidelines set down by the Ministry for Agriculture Food and Fisheries. The crystals were sufficiently stable that, by careful handling, liquid could be drawn off to reduce the chance of the crystal slipping during data collection. In general, the more complete the immersion in mother liquor the better the diffraction. In some cases, tapered quartz capillaries were drawn out and crystals allowed to gently settle into the taper so that data could be collected without removing liquor [a technique developed by T. Richmond (personal communication)].

3. Measurement

Data have been collected from several synchrotrons, with station 9.6 at the Synchrotron Radiation Source (SRS) (Daresbury, UK) providing crucial time to get the project off the ground. The undulator beamline ID2 at the European Synchrotron Radiation Facilty (ESRF, Grenoble, France) was the real powerhouse for the collection of the higher-resolution data essential to the structure determination (Boesecke, 1992; Boesecke *et al.*, 1995. We will make some comparisons between different stations and detectors, although we will concentrate on station ID2 and results from Mar imaging-plate detectors.

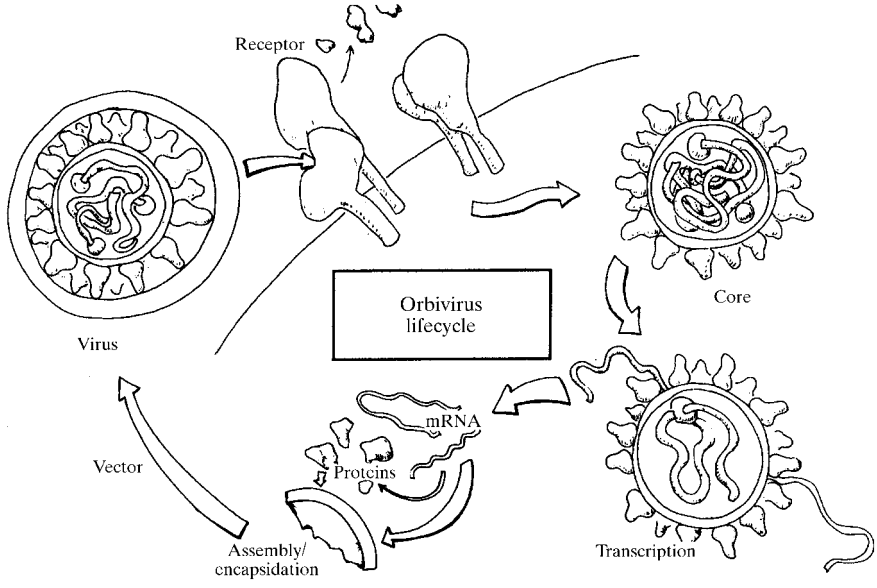

Figure 1
A cartoon of the life cycle of BTV. The virus causes an acute disease in animals such as sheep but is spread between mammalian hosts by an insect vector (Culicoides). The virus replicates in both insect and mammalian hosts and the cartoon could apply to either type of cell.

Diffraction was first demonstrated on PX9.6 at the SRS, a second-generation source upgraded some years ago by the installation of a high-brightness lattice, although the need for higher fluxes for this project has relegated this station largely to a testing role. Data collection on DW21B and DW32 at LURE (Orsay, France), an unreconstructed source with lower flux density, demonstrated the crucial importance of brilliance and provided no advantage over the (much closer) SRS. The high-brilliance beam available on ID2B from the third-generation ESRF allows an image to be recorded in a few seconds, so that over 600 crystals could be examined in a two-day experiment. Other stations, in particular those belonging to the ID14 family at the ESRF, may provide a comparable service in the future.

3.1. *Wavelength*

The wavelength of X-rays used varied between 0.87 Å at the SRS (essentially optimum for the beam optics) to 0.99–1.00 Å at the ESRF and LURE (there were small differences from one visit to the next). The highest fluxes were available at the ESRF operating in two-thirds fill mode, which allowed a beam size as low as 50 μm × 50 μm to be used on beamline ID2. For routine data collection this was increased to about 80 μm × 80 μm to allow more flux for collection to 3.5 Å resolution. These wavelengths allow data collection for most projects to proceed without concern about the amount of air scatter/absorption. If we collect data at a crystal-to-detector distance of 1 m, the transmission through the air (at a wavelength of 1.00 Å) should be about 70%, falling to some 50% at 1.5 m. At present we are aware of only the Photon Factory (Sakabe, 1991) providing a helium path as routine equipment to increase transmission. These losses of signal (and increase in noise due to scatter) are relatively modest; however, very little of the incident beam is scattered by the virus crystal, and the fraction that does contribute to the Bragg diffraction is spread between the many thousand reflections which are simultaneously excited. Thus the inevitably poor signal-to-noise ratio for such data will be further degraded by air scatter from the direct beam, unless considerable care is taken to minimize the pathlength between the guard aperture and the backstop.

3.2. *Optics and collimation*

Fig. 3 presents the beam optics and some beam parameters for ID2. This station, fed by an undulator, provides a beam of great brilliance and low horizontal and vertical divergence (for instance, the horizontal divergence of the beam is roughly 500 times less than that for station 9.6, taking the full fan of radiation). Note in particular the complex arrangement of slits which allow the beam to be defined some distance upstream from the crystal, so that the slits positioned 4 cm from the crystal simply act as guard apertures, producing a beam with very little evidence of parasitic scatter. A nose-piece, approximately 1 cm from the crystal, acts as a final guard aperture. The provision of motorized control of even the guard slits, in conjunction with a number of pin diodes and an X-ray eye camera, allowed precise positioning of the various components, eliminating flare.

Various backstops were designed and tested, since we were concerned with collecting adequate low-resolution data to have a reasonable overlap with the low-resolution information available from electron microscopy. To avoid a long air path for the direct beam the backstop must be rather small. With the well collimated beam on ID2 we currently use a 0.8 mm backstop made of tantallum (although gold also works well) which, positioned 6.5 cm from the crystal, allows us to collect data to a low-resolution limit of ∼110 Å. Note that the thin-walled quartz capillary tubes in which the crystals are mounted can act as cylindrical lenses to such a fine parallel X-ray beam, when the beam glances off the upper or lower surfaces which are close to parallel to the beam. Such flaring cannot be blamed upon the station optics!

3.3. *Detectors*

The vast majority of the data have been recorded using MAResearch 300 mm and 345 mm image plates. For anything other than very low resolution data the full aperture of the detector must be used to enable sufficient solid angle to be sampled at sufficient distance to resolve the diffraction spots. A 345 mm plate with a 100 μm pixel size provides, in principle, the best spot separation, and we

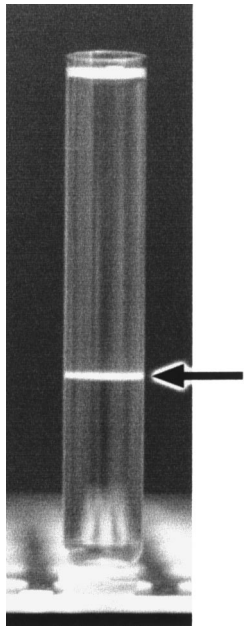

Figure 2
Core particles of bluetongue virus serotype 1 from South Africa (BTV-1 SA), in the final stage of purification, using a self-forming CsCl gradient as described by Mertens *et al.* (1987). The gradient, which contains approximately 10 mg of BTV-1 SA core particles, was centrifuged in a Beckman SW 40 rotor at 34 Kr.p.m. for 24 h at 277 K. The cores formed only one tight band at a density of 1.40 g cm^{-3}, indicating that they have a single density and therefore have a uniform composition of RNA genome segments and viral proteins. No other contaminating bands were detected.

have gathered over 73000 reflections on a single image using this setting (Fig. 4). Despite crystals that often only lasted for a single exposure, we could maintain a collection rate of 2–3 min image^{-1} by pre-mounting crystals on goniometer heads and carefully pre-centring using an optical goniometer (we endeavoured to use random crystal orientations so as to optimize data completeness). Scan and erase times on this setting therefore became the limiting factor and so we examined the effect of different scan rasters on the spot resolution. Fig. 5 presents a comparison of the results of using several X-ray sources and detectors, with images adjusted so that the scale is similar for each. Comparison of Figs. 5(*a*) and 5(*b*) reveals that there is little improvement in scanning at 100 µm instead of 150 µm. To maximize data throughput we therefore often used the coarser raster.

We have gathered a small amount of data on a Quantum4 CCD camera available on PX9.6, SRS. This device has a square active area, made up of 2304 pixels in each direction (each pixel is 81.6 µm across). Not only does such a detector provide a much faster scan cycle than an on-line image plate but it is clear that the effective spatial resolution is excellent (Fig. 5*d*), enabling a greater number of diffraction spots to be packed on a single image. Some test data collections were also made on ID14, EH3 at the ESRF, using Fuji 40 cm × 80 cm image plates (scanned off-line with an EMBL device), which can be mounted side-by-side to give a total active area 0.8 × 0.8 m^2 (composed of 6.4 × 10^7 pixels), allowing high-resolution data collection at long crystal-to-plate distances. Fig. 5(*c*) shows data from this station, which demonstrates the tremendous gains possible in signal to noise by using a very large detector placed far back from the crystal. The basic reason for this is well known: background scatter falls off as $1/D^2$, where D is the crystal-to-detector distance, whereas the diffracted beams fall off as $1/S^2$, where S is the distance of the detector from the effective X-ray source (see §11, Fig. 3). Defining the effective source position can be difficult; however, from the very large distances marked on Fig. 3 it will be obvious that the intensity of the diffracted beams will be very little affected by the small increases in pathlength entailed by moving a detector back by 1 m. Finally, Fig. 5(*e*) shows a row of spots taken from a BTV-10 USA diffraction image, demonstrating that it is straightforward to resolve spots at spacings of 1/1584 Å^{-1}.

3.4. *User-defined parameters*

In general, crystal-to-plate distances used were chosen to be the longest possible compatible with the resolution range desired. The highest-resolution reflections measured (3.50 Å) were collected with a crystal-to-plate distance of 680 mm and the 300 mm MAR detector swung out to an angle of $2\theta = 4^\circ$. This method collected a solid angle of only 32° of data in the 3.60–3.55 Å range. Additional 3.55 Å data were collected using the 345 mm plate and 100 µm pixel size at a distance of 600 mm with no swing angle, albeit with a greatly reduced spot separation. For low-resolution data, distances of 1000 or 1050 mm were used. 1000 mm gives approximately a 1.7-fold improvement in the ratio of signal to noise over 600 mm. In the case of BTV-10, the large unit-cell dimensions gave no option but to use 1050 mm (the maximum possible at ID2).

The choice of oscillation range was dictated by spot separation at the edge of the image plate. For the 3.5 Å

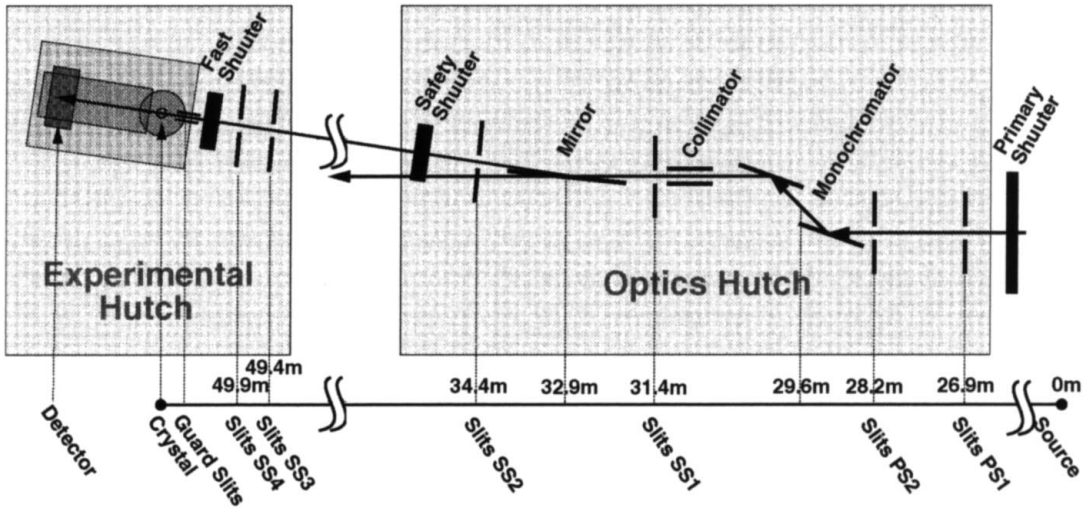

Figure 3
Plan of the elements that define the beam on the high-brilliance undulator beamline ID2, ESRF. The low beam divergence, coupled with the use of guard slits and beam defining slits from the source and spread over 23 m (27–50 m from the source, with the final guard slits as close as possible to the crystal, as discussed in the text, to minimize scatter). This results in an X-ray beam that is close to parallel. The improvement in the signal-to-noise ratio possible by the pushing back of the detector (as described in the text) is dependent on a long distance between the crystal and the effective source of X-rays. The effective source position will clearly be determined by the nature and positions of the optical elements. For ID2, the great distance between the toroidal mirror, the last optical element, and the crystal ensures that this aspect of the station design is not limiting.

data collected with a 4° swing angle, an oscillation range of 0.25° was used. For the 3.55 Å data collected with no swing, a range of 0.2° was necessary. At low resolutions a range of 0.4° was chosen. Fortunately, the mosaic spread of native BTV crystals was small, generally 0.06–0.14°. This allowed a reasonable yield of useful data from each image using the data-analysis scheme described below.

Exposure times of between 5 s and 30 min have been used, dependent mainly on beam strength but also on the particular resolution sought. At the ESRF, exposures in the range 5–90 s were required (exposures in excess of about 10 s were usually with the machine operating in 16-bunch operation, where the intensity is reduced by a factor of about three compared with two-thirds fill). At the SRS, exposures were in the range 1–10 min. In order to measure even medium-resolution data on this station, the width of the fan of radiation incident upon the horizontally focusing monochromator was reduced to about one-third of its normal value, with a corresponding reduction in flux. At LURE, the less-brilliant source required an absolute minimum exposure time of 20–30 min (in this case we used a helium path to reduce air scatter). The effective *B*-factor for the diffraction was rather high (the final data set was sharpened, prior to map calculation, by applying an inverse *B*-factor of 44.5 Å^2). Thus it was difficult to record higher-resolution data before the crystal was destroyed. We have investigated methods for cooling the crystals; however, the usual protocols proved ineffective. We therefore worked with crystals cooled to approximately 277 K using an FTS device.

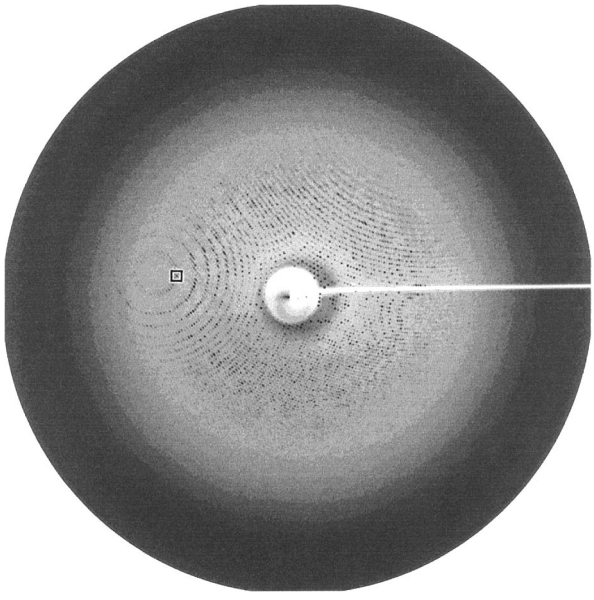

Figure 4
Diffraction pattern from a crystal of BTV-1 SA, collected on a Mar 345 imaging-plate device with a pixel size of 100 µm, at ID2. The crystal-to-detector distance was 600 mm and the wavelength was 0.99 Å, which gives a nominal resolution at the edge of the plate of 3.55 Å. The crystal was oscillated through 0.2°. The small box defines the area shown in Fig. 5(*b*).

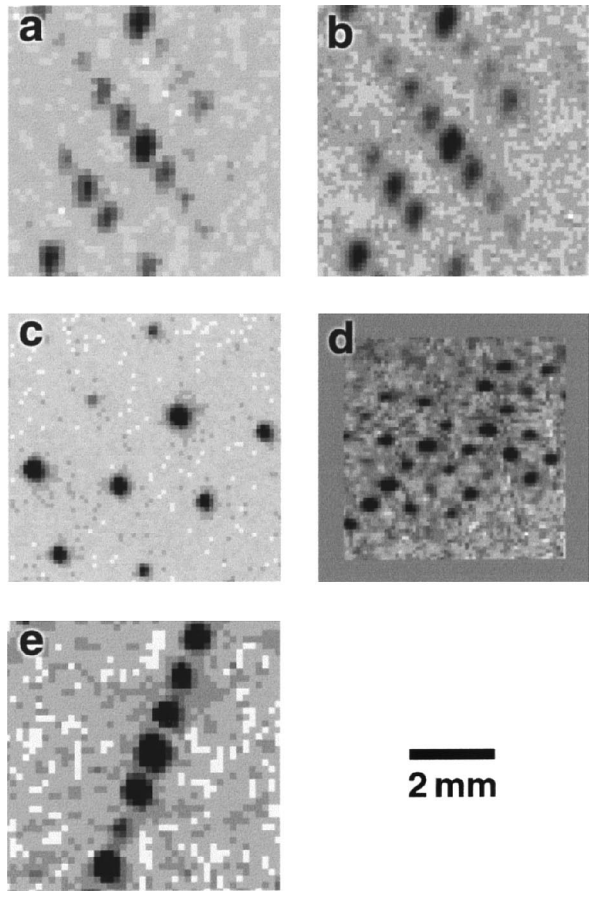

Figure 5
Close-ups of diffraction patterns from BTV crystals, collected on several different detectors/scanners at different beamlines at the ESRF and the SRS. (*a*) Diffraction from a BTV-1 SA crystal collected on a Mar 345 imaging plate using a pixel size of 150 µm. The crystal-to-plate distance was 600 mm, the wavelength was 0.99 Å and the crystal was oscillated through 0.2°. (*b*) The same image as (*a*) but recorded with the pixel size set to 100 µm, showing the improvement in spot separation. (*c*) Image recorded on a large 40 cm × 80 cm imaging plate using the EMBL off-line scanner, on EH3 ID14 at the ESRF. The crystal-to-plate distance was 1250 mm, the crystal was oscillated through 0.25° and the wavelength was 0.99 Å. Note the remarkable separation of the spots and the clear improvement in signal to noise (the background is essentially flat) with the sample-to-detector distance set to over 1.2 m. The resolution at the edge of the plate was 3.6 Å, comparable with Figs. 5(*a*) and 5(*b*). (*d*) Image taken from a BTV-1 SA crystal using an ADSC Quantum 4 2 × 2 CCD at beamline 9.6 at the SRS. The crystal-to-plate distance was 400 mm and the crystal oscillation angle was 0.25°. The pixel size of the ADSC CCD is 81.6 µm and the image has been scaled down accordingly. Note that even for an X-ray source such as beamline 9.6, with a far higher beam divergence than ID2, the spot separation with the crystal-to-plate distance of 400 mm is extremely good, presumably reflecting the very small point-spread function of the ADSC detector compared with the Mar 345 imaging plate. (*e*) Close up of a diffraction image from a crystal of BTV-10 USA, taken on ID2 using a MARresearch 300 mm imaging plate with a 150 µm pixel size. The separation of the spots within the row is *c**, *i.e.* 1/1584 Å^{-1}, and so the detector distance was maximized to 1050 mm. The crystal was oscillated through 0.25° and the resolution at the edge of the plate is about 6.5 Å.

One important advantage of the small beam size was the ability to collect data from more than one position per crystal. With crystals occasionally reaching up to 0.6 mm in the longest dimension, we were able to collect from as many as 12 positions from some crystals. The quality of data tended to decrease from each successive position, indicating that radiation damage was spread throughout the crystal. Inspection of the crystal revealed the irradiated portion as an opaque tube penetrating the crystal and quite often this damage was accompanied by the appearance of major cracks. Nevertheless, for some large crystals we were able to obtain useful data from several positions (non-contiguous oscillation ranges were used to ensure the maximum number of reflections were measured). Where crystal size did not allow for multiple positions, it was sometimes possible to collect up to six consecutive images using low-dose exposures and consequently gathering only low-resolution data. Only a very small number of the native BTV-1 crystals diffracted to 3.5 Å. A significant fraction of all the crystals exposed were too disordered to give any data at all. In total, over 3000 images have been collected from native BTV and derivatized crystals.

4. Integration

Data were indexed and integrated using versions of *DENZO* from the package *HKL* (Otwinowski & Minor, 1997). Images generally required indexing individually, a task greatly simplified by the robust auto-indexing algorithm of *DENZO*. With closely packed images, accurate knowledge of the direct-beam position was essential (often determined from powder diffraction rings). Determining the orientation of the crystal was then unproblematic. Images were measured in the primitive orthorhombic space group *P*222 (systematic absences were removed at a later stage). The spot size used for integration varied slightly with the crystal-to-plate distance, and consequent implications for spot separation. A radius of 0.4 mm was used for a distance of 1000 mm (~6.5 Å at the edge of the detector), with guard radius 0.55 mm and background box 3.0 × 3.0 mm^2. A radius of 0.35 mm was used for the data collected at 600 mm (~3.55 Å at the edge), combined with guard radius 0.45 mm and box 3.0 × 3.0 mm^2, in order to reduce the number of overlapped reflections at high resolution. In general, a considerable number of neighbouring spots fall within the background region for each spot, so that to ensure a reasonably reliable estimate for the background level the spot box was made as large as possible. The majority of the other parameters were left as the default values.

After integration and before scaling, the high-resolution limit for each image was determined dynamically using *TRIM_DENZO* (D. I. Stuart, unpublished program). Reflections were divided into resolution shells, and the shells were examined, starting from that at highest resolution working inwards, discarding data until a shell was encountered for which greater than 20% of the reflections had $I/\sigma(I) > 2$.

5. Scaling

Data were scaled using versions of *SCALEPACK* from the package *HKL* (Otwinowski & Minor, 1997). Very large versions were required, as the native dataset contained 919 images and 211568019 reflections. Scale factors and individual *B*-factors were determined, normalized to one of the best images. The error model was chosen to give χ^2 values close to unity and data were rejected according to the standard Bayesian test. Unit-cell parameters were optimized within blocks of images collected on the same trip (to allow for slight errors in the wavelength determination). Scaled but unmerged data were further processed using *POST* (D. I. Stuart, unpublished program) to treat partially recorded reflections. Reflections for which the fraction recorded exceeded 0.6 were scaled up and reclassified as fully recorded; the others were discarded. The remaining data were re-scaled, merged and passed to *TIDY* (D. I. Stuart, unpublished program) which analysed data in resolution shells, removing outliers from the intensity distribution. The resultant native dataset was 57.0% complete between 105 and 3.5 Å, with a final $R_{\rm merge}$ of 36.6% and $\langle I\rangle/\langle\sigma(I)\rangle = 2.06$. Structure factor amplitudes were calculated from the intensities using the *CCP*4 program *TRUNCATE* (French & Wilson, 1978). The native dataset contained 3388940 reflections. A unit cell of a = 795.58 Å, b = 821.78 Å, c = 753.26 Å was chosen as a suitable compromise between the various similar solutions found during scaling. The space group proved to be $P2_12_12$. The scaling of the BTV-10 USA data set proceeded in a similar manner, except that a post-integration correction for spot overlap was performed (Bourgeois *et al.*, 1998).

6. Model

An atomic model was built for the outer layer of the core particle, by fitting the crystal structure of the isolated VP7 trimer into a 23 Å resolution cryo-electron microscopic reconstruction (Grimes *et al.*, 1995, 1997). There are 13 monomers of VP7, arranged as 13/3 trimers, in the viral asymmetric unit, which, on application of the full icosahedral symmetry, generates the entire layer. A real-space steepest-descent refinement procedure [program *GAP* (D. I. Stuart & J. M. Grimes, unpublished)] optimized the orientations and positions of the 13/3 trimers. The resultant model was used for molecular replacement studies.

7. Molecular replacement

Packing and symmetry considerations dictate that the crystallographic asymmetric unit contains half a particle, with an icosahedral twofold axis aligned along the *c*-axis. Only two degrees of freedom remain: the orientation of the particle around the *c*-axis and its position along that axis.

The orientation of the particle was evident from self-rotation functions calculated using *X-PLOR* (Brunger, 1992) (Fig. 6*a*). Use of a large integration radius (using vectors between 200 and 600 Å in length) and a large number of Patterson peaks (125000 peaks) lead to a sharp function showing icosahedral twofold axes inclined at some 2.3° to the crystallographic axes. Fine angular grid searches refined this to 2.14°. A simple translation search along the *z*-axis gave the position of the particle. Initially the model was moved along the *z*-axis in steps of 2 Å (using data between 60 and 30 Å). To make the computation tractable our molecular replacement model only included every tenth Cα atom (132600 in total). This gave a very clear solution (see Fig. 6*b*). In grid searches using only very low resolution data the algorithm used to generate calculated structure factors becomes inappropriate, since a typical choice of grid for the FFT calculation is sufficiently coarse that most of the atoms fail to contribute to any grid point. By using a very large anti-aliasing *B*-factor (BSCAL in *X-PLOR*) of 1500 Å^2 the atoms were expanded to ensure that they contributed to at least one grid point. Since the model was derived from an electron micrographic reconstruction the exact scale of the model was uncertain. A procedure for scaling the virion transform was implemented in *X-PLOR* which indicated that the appropriate scale factor was 0.995 (Fig. 6*c*). Finally, an iterative series of rigid-body refinements were performed, to optimize both the orientation and position of the particle (by treating the half of the particle that comprises the crystallographic asymmetric unit as a rigid body) and also, holding the NCS operators fixed, treating each trimer within the icosahedral asymmetric unit as a rigid body to refine the internal structure of the icosahedral asymmetric unit. The final correlation coefficient using all available data between 60 and 12 Å was 0.35, and remained positive at 12 Å, despite the fact that the resolution of the original reconstruction only extended to 23 Å resolution. This model, containing only the outer VP7(T13) layer of the core, provided starting phases.

The determination of the particle orientation and position in the BTV-10 USA crystals was more challenging; this is described briefly by Gouet *et al.* (1999). Here we simply show the $\kappa = 72°$ section of the self-rotation function (Fig. 7). The combination of high crystal symmetry and weak incomplete data (54% complete to 6.5 Å, with a merging *R* of 34%) produce a complex function, which was satisfying to interpret (the calculated peaks for the deduced particle orientation, reduced to space group *P*1, are shown superimposed in blue).

8. Phasing

The initial phases were improved using a protocol which used both real- and reciprocal-space methods. Phases to 12 Å resolution were refined by cyclic real-space averaging and solvent flattening. Rigid-body refinement of the model then provided phase information to 6 Å, which was

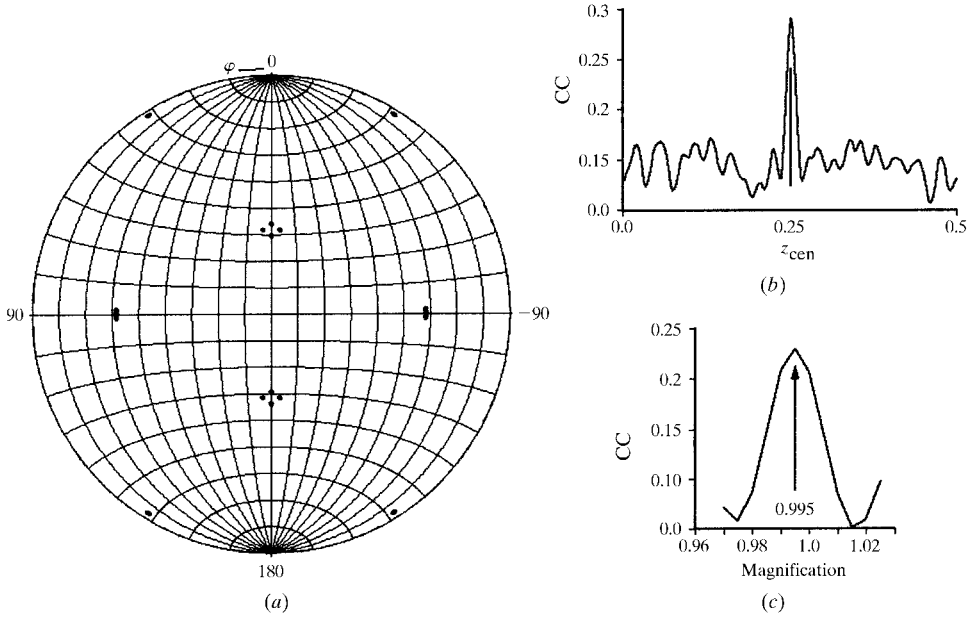

Figure 6
Molecular replacement solution for the core particle of BTV-1 SA. (*a*) The $\kappa = 72°$ section of the self-rotation function. Patterson vectors between 600 and 200 Å in length were used in the integration, and the 125000 highest peaks were used in the search. The sharp peaks define the orientations of the fivefold axes extremely accurately. (*b*) The translation search of the crude model along the *z*-axis. Data between 60 and 30 Å were used in the calculation and the search was from 0 to 0.5 in steps of 2 Å along the *z*-axis. (*c*) The amplification search for optimization of the cryo-EM data to the crystallographic data between 25 and 20 Å. A grid search was used where model coordinates were scaled by a factor of 0.96 to 1.03 in steps of 0.005, showing a clear peak with a scale factor of 0.995. CC is the linear correlation coefficient calculated between observed and calculated structure factors, z_{cen} is the fractional *z* coordinate for the particle centre and magnification is the magnification of the cryo-EM data.

combined with the extant 12 Å phases. The real-space map modification protocols then rapidly produced a high-quality electron density map at 6 Å resolution. This was much less laborious than conventional incremental phase refinement and extension in real space. The map was of excellent quality, allowing atomic models for the secondary structural features of the underlying layer of VP3 to be constructed, refined, along with the existing models for

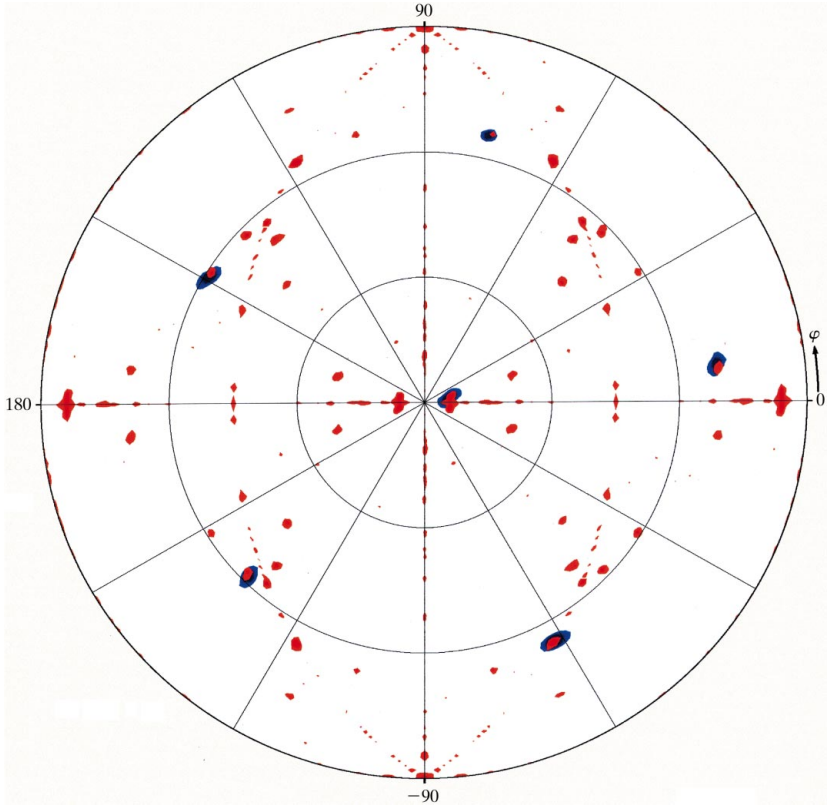

Figure 7
$\kappa = 72^\circ$ section of the self-rotation function, for native BTV-10 USA X-ray data calculated in point group *P*422 (in red) and for the BTV-1 SA model calculated in point group *P*1. The integration radius of Patterson data used was from 600 to 200 Å, and the 150 000 highest peaks were used.

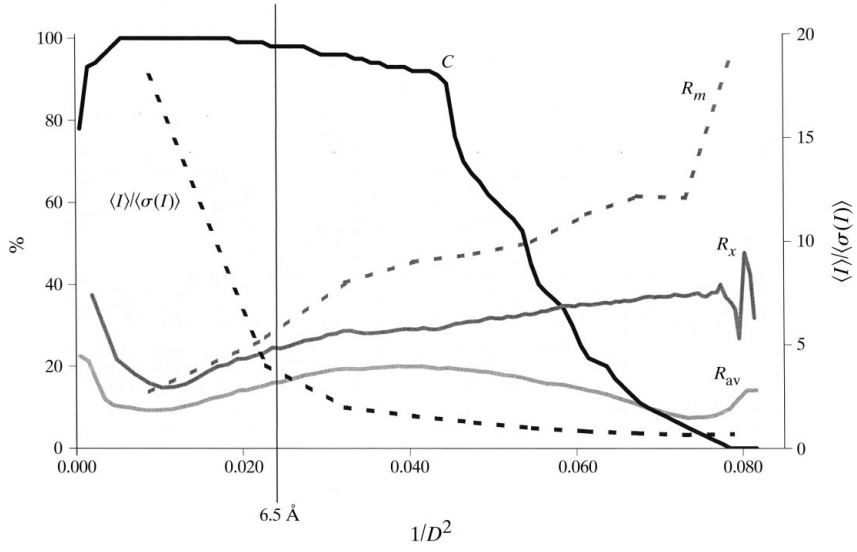

Figure 8
Graph showing several *R*-factors and data completeness (*C*) with respect to resolution. R_m is the standard merging *R*-factor on intensities, R_x is the conventional *R*-factor for the final model, calculated using *X-PLOR* (Brunger, 1992), R_{av} is the *R*-factor between the observed structure factor amplitudes and those derived from inversion of the averaged solvent-flattened map, $\langle I\rangle/\langle\sigma(I)\rangle$ is the mean standard intensity divided by the mean error estimated by *SCALEPACK* (Otwinowski & Minor, 1997). Note how the averaging and refinement *R*-factors are notably better than *R*-merge, indicating that there is useful information in seemingly poor-quality data.

VP7(T13) as rigid bodies, firstly against data at 6 Å and then using data to 3.8 Å (the limit of data at the time). This allowed phases to 3.8 Å to be calculated and improved once again by real-space 30-fold averaging, solvent flattening and automatic envelope refinement.

9. Model building

The resultant electron density maps were of sufficient quality that the model for the two molecules of the 901 residue VP3(T2) protein were built unambiguously in a few days using *FRODO* (Jones, 1985) on an Evans & Sutherland ESV10 graphics workstation. It was clear from the electron density even at 3.8 Å that there were several errors in the sequence (A. M. Wade-Evans, unpublished data) which were corrected by reference to the sequences of other serotypes of bluetongue virus.

10. Refinement

Despite the limited resolution of the data set (some data measured to 3.5 Å, but the data set is incomplete and the data very weak at this resolution; see Fig. 8), the structure was refined using *X-PLOR*. Strict NCS constraints were imposed, maintaining a ratio of observations to refined atoms of 67. Refinement (positional and restrained isotropic *B*-factors) was interleaved with rigid-body refinement to optimize the NCS operators, phase calculation and phase refinement by classic real-space averaging procedures. The procedure was well conditioned resulting in an overall *R*-factor of 26% and a model for which only 1% of the residues fell in disallowed regions of the Ramachandran plot (Laskowski *et al.*, 1993). As seen from Fig. 8, the final averaging *R*-factors are considerably lower than the *X-PLOR R*-factor, suggesting the model is not optimum. One reason for this is the presence of ordered protein and dsRNA within the capsid (Gouet *et al.*, 1999). Nevertheless, the *X-PLOR R*-factor is satisfyingly lower than the *R*-merge for the data set (Fig. 8), due in part to the use of structure factor intensities instead of amplitudes in the *R*-factor calculation.

11. Discussion

The third-generation synchrotrons, often operating at high energies (6–8 GeV) and equipped with undulator insertion devices, provide X-ray beams ideally suited to the analysis of crystals of very complex macromolecular assemblies. The X-ray detectors that are routinely available have many desirable properties for measuring weak noisy crowded diffraction patterns, but unfortunately no single detector combines all these properties. Nevertheless, the BTV analysis shows that much can already be achieved. As more challenging biological systems are targeted, there will be an increasing need to define the biochemical components and assemble them in a precise fashion. There is an inherent physicochemical problem in forming the crystal lattice. The forces stabilizing the lattice are surface interactions which increase much more slowly with particle size than the dispersive effects, which will tend to scale with molecular volume. Thus the total surface-area-rendered solvent inaccessible by the crystal contacts within the BTV-1 SA crystal lattice is 7000 Å^2, less than an order of magnitude greater than that responsible for the formation of typical ligand–receptor interactions, where the molecular mass of each component is some three orders of magnitude less than that of the BTV core. If we compare the number of atoms involved in unique contacts it transpires that they are less in number than those involved in holding crystals of HIV-1 RT together (Esnouf *et al.*, 1998), where the crystal asymmetric unit is over 100 times smaller. Not only is the BTV lattice fragile but the particle itself has some flexibility. Fig. 9 shows the distribution of *B*-factors around the particle and it is clear that the fivefold apices are particularly mobile, along with most of the outer surface. In this situation it is not surprising that the diffraction becomes weak at medium resolution. Finally, we detect a slow ageing of the crystals, so that the unit-cell dimensions vary over

Figure 9
Image of the core particle of BTV-1 SA colour-coded by *B*-factor. Blue indicates a low *B*-factor (<10 Å^2) through to yellow indicating a high *B*-factor (>150 Å^2). Note the increase in *B*-factor values of protein towards the icosahedral fivefold axes, as well as in the upper domains of the outer layer of VP7. Drawn with Bobscript (Esnouf, 1997) and rendered with POVray (Persistence of Vision, http://www.povray.org/).

time. It is likely that many such complex systems will harbour their own particular problems for the structural biologist, problems that will often stretch the available synchrotron beamlines to their limits.

We thank the SRS, LURE, ESRF and EMBL for their assistance in data collection; the disease security officers D. Goodridge OBE, S. Williams, A. Meyer and P. Wilkinson; M. Pickford for technical assistance; R. Bryan, K. Measures and R. Esnouf for computing; S. Lee for assistance with figures. This work has been given long-term support by the BBSRC, MRC and EC; RM was supported by a C. J. Martin Fellowship from NHMRC Australia; PPCM and JNB are supported by MAFF.

References

Boesecke, P. (1992). *Rev. Sci. Instrum.* **63**, 438–441

Boesecke, P., Diat, O. & Rasmussen, B. (1995). *Rev. Sci. Instrum.* **66**, 1636–1638

Bourgeois, D., Nurizzo, D., Kahn, R. & Cambillau, C. (1998). *J. Appl. Cryst.* **31**, 22–35.

Brunger, A. T. (1992). *X-PLOR.* Version 3.1. Yale University Press.

Burroughs, J. N., Grimes, J. M., Mertens, P. P. C. & Stuart, D. I. (1995). *Virology*, **210**, 217–220.

Burroughs, J. N., O'Hara, R. S., Smale, C. J., Hamblin, C., Walton, A., Armstrong, R. & Mertens, P. P. C. (1994). *J. Gen. Virol.* **75**, 1849–1857.

Esnouf, R. M. (1997). *J. Mol. Graph.* **15**, 133–138.

Esnouf, R. M., Ren, J., Garman, E. F., Somers, D. O. N., Ross, C. K., Jones, E. Y., Stammers, D. K. & Stuart, D. I. (1998). *Acta Cryst.* D**54**, 938–953.

French, S. & Wilson, K. (1978). *Acta Cryst.* A**34**, 517–525.

Gouet, P., Diprose, J. M., Grimes, J. M., Malby, R., Burroughs, J. N., Zientara, S., Stuart, D. I. & Mertens, P. P. C. (1999). *Cell*, **97**, 481–490.

Grimes, J. M., Basak, A. K., Roy, P. & Stuart, D. I. (1995). *Nature (London)*, **373**, 167–170.

Grimes, J. M., Burroughs, J. N., Gouet, P., Diprose, J. M., Malby, R., Mertens, P. P. C. & Stuart, D. I. (1998). *Nature (London)*, **395**, 470–478.

Grimes, J. M., Jakana, J., Ghosh, M., Basak, A. K., Roy, P., Chiu, W., Stuart, D. I. & Prasad, B.V.V. (1997). *Structure*, **5**, 885–893.

Jones, T. A. (1985). *Diffract. Methods Biol. Macromol.* **115**, 157–171.

Laskowski, R. A., MacArthur, M. W., Moss, D. S. & Thornton, J. M. (1993). *J. Appl. Cryst.* **26**, 283–291.

Martin, L. A., Meyer, A. J., O'Hara, R. S., Fu, H., Knowles, N. J. & Mertens, P. P. C. (1998). *Ach. Virol.* S**14**, 281–293.

Mertens, P. P. C., Burroughs, J. N. & Anderson, J. (1987). *Virology*, **157**, 375–386.

Otwinowski, Z. O. & Minor, W. (1997). *Macromolecular Crystallography*, edited by J. W. Carter Jr. & R. M. Sweet, pp. 307–326. San Diego: Academic Press.

Ramadevi, N., Burroughs, N. J., Mertens, P. P. C., Jones, I. M. & Roy, P. (1998). *Proc. Natl Acad. Sci. USA*, **95**, 13537–13542.

Sakabe, N. (1991). *Nucl. Instrum. Methods Phys. Res. A*, **303**, 448–463.

Stauber, N., Martinez-Costas, J., Sutton, G., Monastyrskaya, K. & Roy, P. (1997). *J. Virol.* **71**, 7220–7226.

Urakawa, T., Ritter, D. G. & Roy, P. (1989). *Nucleic Acids Res.* **17**, 7395–7401.

Van Dijk, A. A. & Huismans, H. (1980). *Virology*, **104**, 347–356.